Additive Manufacturing of Shape Memory Thermoset Composites with Directional Thermal Conductivity

Yinglun Hong,* Itxaso Azcune, Alaitz Rekondo, Tianhui Jiang, Shitong Zhou, Tristan Lowe, and Eduardo Saiz

Shape memory epoxy vitrimers and their composites are candidate materials for multiple engineering applications due to the commercial availability of their precursors combined with their functionality, mechanical properties, and recyclability. However, the manufacturing of vitrimer composites through conventional mould-casting limits the flexibility in the design of complex parts. In this work feedstock inks are formulated based on reduced graphene oxide and hexagonal boron nitride (hBN) to 3D-print epoxy vitrimer-based composites by direct ink writing (DIW). The introduction of hBN platelets (up to 22 vol.%) and their alignment during printing enhances the fracture resistance of the material and induces directional thermal transport. The in-plane thermal conductivities ($3\ \text{W m}^{-1}\ \text{K}^{-1}$) are nearly one order of magnitude higher than the matrix material. The high conductivity results in faster actuation times and can be combined with the printing process to build structures designed to manage heat flow.

1. Introduction

Materials able to combine structural and functional capabilities with the ability to modify their shape in response to external stimuli could enable new technologies in a wide range of fields, from health care to energy or transportation.[1] Shape shifting could reduce drag and fuel consumption in vehicles[2] or can be used to

Y. Hong, T. Jiang, S. Zhou, E. Saiz
Centre for Advanced Structural Ceramics
Department of Materials
Imperial College London
London SW7 2AZ, UK
E-mail: yinglun.hong15@imperial.ac.uk
I. Azcune, A. Rekondo
CIDETEC
Basque Research and Technology Alliance (BRTA)
Paseo Miramón, 196, Donostia-San Sebastián 20014, Spain
T. Lowe
Henry Moseley X-ray Imaging Facility
Photon science Institute
The University of Manchester
Manchester M13 9PL, UK

accomplish tasks in hard to reach places for applications such as actuators,[3] medical devices,[4] and self-deployable structures for spacecrafts.[5] The interest has generated a significant amount of research on the development of responsive shape memory compounds, from alloys to polymers, able to recover their original shape after deformation.

An important step forward in the design of adaptive materials has been the development of thermally responsive shape memory polymers (SMP). Their working principle relies on the ability of the polymers to recover their original permanent state after having passed through a temporary, but stable, fixed state following exposure to temperatures above their glass transition, T_g. SMPs have significant advantages compared to shape-memory alloys in terms of weight and processing simplicity. There are also concerns regarding the high programming temperature (hundreds of degrees Celsius) for alloys.[6] In addition, the functionalities that could be obtained through the combination of SMPs with other materials in composites could open new technological opportunities. For example, there is an increasing interest in structures for thermal management in areas such as electronics.[7] Here, the combination of composites and shape actuation could create new possibilities to direct heat flow.[8] However, there still exist significant limitations for the technological application of SMPs.[9] At the moment, many shape memory polymers exhibit relatively slow recovery and reaction times.[10] Furthermore, their mechanical properties, in particular their fracture resistance, are far from those needed in load-bearing applications.[11] In this respect, thermoset SMPs and their composites are generally preferable to thermoplastics due to their chemical and temperature resistance and better mechanical performance. However, the fabrication of complex thermoset structures using conventional mold-casting is a challenge. In addition, the recovery or repair of thermoset polymers is a problem that needs to be addressed in order to enable more sustainable practices. These challenges demand new polymer compositions and shaping technologies. Additive manufacturing could enable the fabrication of on-demand complex parts. As an added advantage, the additive manufacturing of SMP composites opens the possibility of manipulating structure from the micro to macro levels to fabricate structural metamaterials combining shape memory capabilities with unique mechanical and functional response. However, unlike thermoplastics that can
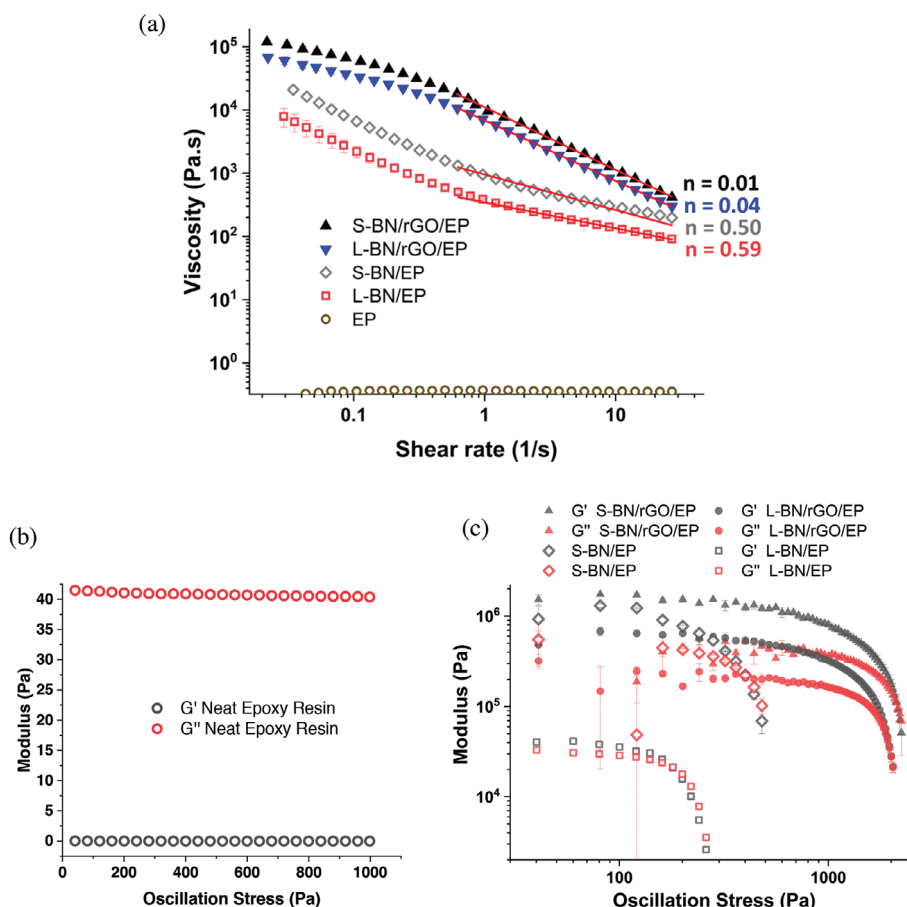
Figure 1. Rheology measurements of neat EP and EP-based inks: a) Flow ramps showing the dependence of the fluid viscosity with shear rate ramp. Power law fittings are shown in red lines ($R^2 > 0.98$). Storage and loss modulus of b) uncured neat EP and c) hBN/EP pastes.

be 3D-printed easily using the well-developed fused deposition modelling (FDM) technique,[12–14] cured thermosets are difficult to adapt to existing technologies.

In this work we use reduced graphene oxide (rGO) as an additive to manipulate the rheology of an epoxy resin vitrimer (EP) prior to curing. The vitrimer comprises two monomers: bisphenol A diglycidyl ether (DGEBA) and Poly(propylene glycol) diglycidic ether (DGEPPG); and one hardener: 4-Aminophenyldisulfide (4-AFD), to form a disulphide containing epoxy network that combines a shape memory response with the capability for reprocessing.[15] Since thermoset polymers are not intrinsically 3-D printable using continuous extrusion, additives (e.g., nanoclay,[16] fumed silica,[12] carbon nanotubes[13]) are often introduced to modify their rheology, or extrusion is combined with simultaneous curing during printing.[17,18] The challenge is to find additives that do not have a detrimental effect on the final properties of the material and that could even add additional functionalities. We use very small amounts of rGO to enable the formulation of shear-thinning pastes with the yield stress required for the direct ink writing at room temperature of complex parts that can be subsequently cured. In addition, hexagonal boron nitride (hBN) platelets are added to the paste to enhance the thermal conductivity (and consequently the shape recovery speed) and fracture resistance of the materials. The orientation of

the platelets during the extrusion-based printing process can be used to achieve directional thermal conductivity and build thermal metamaterial structures. Here, we analyze the role of rGO on the rheology of printing pastes, and the evolution of the structure and properties of the final materials as a function of their composition and the printing conditions. The objective is to provide a path toward the printing of thermoset, shape memory parts that could address some of the existing challenges in the field.

2. Results and Discussion

2.1. Printability

In order to fabricate hBN/EP vitrimer composites through direct ink writing (DIW) it is necessary to use extrudable printing inks with a shear thinning behavior. The equilibrium storage moduli (G'_{eq}) in the linear region and the flow points have to be high enough to enable shape retention in the printed part.[14] The uncured EP is a Newtonian fluid whose viscosity is as low as 0.3 Pa·s and independent of shear rate (**Figure 1**). The composition of the EP-based ink was adjusted and aimed to maximize the hBN content and to ensure a good printing performance. Based on our experimental observations (Figure S4, Supporting Information), the maximum amount of hBN that can be fully

**ADVANCED
SCIENCE NEWS**

www.advancedsciencenews.com

**ADVANCED
FUNCTIONAL
MATERIALS**

www.afm-journal.de

incorporated into the EP to form a homogeneous slurry was ≈27 vol.%. The addition of rGO decreases this content to ≈22 vol.%. In this report, we studied four ink formulations based on EP, including slurries consisting of 27 vol.% of smaller-sized hBN platelets (d(50) = 6 μm, S-BN), (S-BN/EP), or 27 vol.% of larger-sized hBN platelets (d(50) = 25 μm, L-BN), (L-BN/EP), and slurries containing 22 vol.% S-BN and 1.8 wt% rGO (S-BN/rGO/EP) or 22 vol.% L-BN and 2.4 wt% rGO (L-BN/rGO/EP). The hBN content was reduced in pastes with rGO to ensure homogeneity after mixing. Pastes with other hBN/rGO ratios (more hBN and less rGO) have been attempted, but they are either too grainy and inhomogeneous (Figure S4, Supporting Information), or do not possess sufficient shape retention capability when printing (Figures S8 and S9, Supporting Information). The addition of solids to the vitrimer led to a shear-thinning behavior with viscosity decreasing with increasing shear rate. The pastes have higher viscosities, particularly those containing rGO. At a shear rate of 1 s^{-1}, the viscosities of these inks are five orders of magnitude higher than those of pure EP and an order of magnitude higher than those of EP inks containing only hBN.

These EP-based pastes are pseudoplastic fluids whose flow behavior is usually described using the Herschel-Bulkley model:

$$\tau = \tau_y + K\dot{\gamma}^n \tag{1}$$

where τ, τ_y, K, $\dot{\gamma}$, and n are the shear stress, yield stress, viscosity coefficient, shear rate, and shear-thinning coefficient respectively. However, fitting of flow sweep data to the model is affected by transient effects at low shear rates and slippage between the fluid and the parallel-plate geometry at high shear rates. A power law fitting ($\eta = K\dot{\gamma}^{n-1}$, where η represents the viscosity) at intermediate shear rates is often used to avoid inaccuracies.[15] Using this fitting between shear rates of 0.5 and 30 s^{-1}, the S-BN/EP and L-BN/EP fluids exhibited comparable shear-thinning coefficients of 0.50 and 0.59, respectively. The addition of rGO increases the viscosity and lowers the shear thinning coefficient ($n = 0.01\text{-}0.04$).

Oscillatory amplitude sweeps were done to evaluate the printability of the pastes. The uncured EP exhibited a liquid-like behavior with a constant higher loss modulus (G'') compared to its storage modulus (G') through the whole range of oscillation stresses (Figure 1b). The EP-based hBN pastes, on the other hand, exhibited a solid-like to liquid-like transition. The G' value was dominant at low oscillation stresses, but it became lower than the G'' value at higher stresses. The crossover points of the G' and G'' curves were used to identify the flow points (stress at the flow point, τ_f, also referred to as the flow stress or yield stress) of the inks. The inks containing rGO required high stresses, over 2000 Pa, to reach their flow points, whereas those without rGO required much lower stresses to initiate flow, 180 Pa for the L-BN/EP ink and 420 Pa for the S-BN/EP one (Figure 1c). The stress at which G' = 90%G'$_{eq}$ is the yield point (τ_{yp}) of the paste (Table S1, Supporting Information). The τ_{yp} values of S-BN/EP and L-BN/EP were ≈100 Pa, while S-BN/rGO/EP and L-BN/rGO/EP have higher yield points, over 300 Pa (Table S2, Supporting Information).

Five-step oscillatory sweeps were performed to gain a deeper understanding of the structural stability of the inks.[14a,19] The first step is a time sweep at a very low strain to stabilize the structure and measure the storage modulus in the linear region (G'$_0$).

The second step is an oscillatory sweep with ramping frequency from 0.5 to 50 Hz at a low fixed strain of 0.05%, to assess the long-term stability of the ink. The third step is the same as the first step, which is done to condition the fluids. The fourth step is an amplitude sweep which disrupts the original structure of the pastes by bringing them beyond their flow points. The final step is another time sweep, same as the first and third steps, to evaluate the extent and the rate of structural recovery after breakdown in the previous amplitude sweep.[14a] EP-based slurries containing hBN and rGO exhibit relatively stable G'>G'' during the first sweep, indicating their solid-like behaviour at the almost stationary state, while for the S-BN/EP and L-BN/EP slurry a transition from viscous (G''>G') to elastic (G'>G'') response was observed in the initial data points. In addition, the value of G'$_0$ for L-BN/EP (10^4 Pa) was one to two orders of magnitude lower that for the other pastes. The structure of the inks without rGO changed during the frequency sweep, and G'' became dominant at high frequencies, whilst for inks modified with rGO the storage modulus remains dominant and both G' and G'' increase slightly with frequency as expected from a gel.[20] All the pastes recover their solid-like behavior instantly upon strain removal. Their elastic properties (G') are dominant in the final step. The average value of storage modulus in the last step, G'$_{step 5}$, was compared with G'$_0$. Within the measured time range, all inks exhibit a partial recovery with $\frac{G'_{step 5}}{G'_0}$ <50% (**Figure 2**). The recovery of the S-BN/EP slurry is the lowest and its viscous properties (G'') were dominant at the beginning of step 5, the values of G'' and G' remained very similar after 100 s.

To visualize the printing performance of each ink and correlate it to their rheology, flat rectangular bars with a pre-designed cross-sectional area of 25.3 mm^2 in computer-aided design (CAD) were printed and cured under the same conditions. The ratio between the measured area of each printed object (Figure S7, Supporting Information) to the theoretical area, A/A_{th}, reflects the fidelity of the ink formulation. The A/A_{th} values for bars printed with inks containing rGO were >90% while they are ≈60% for those printed with S-BN/EP and L-BN/EP inks.

A feed-stock paste for DIW is extruded continuously and should be self-supportive after deposition. The uncured EP was a Newtonian liquid which, intrinsically, is not 3D printable. The incorporation of hBN and rGO changes the behavior toward a shear thinning gel that behaves as a solid at low stresses and as liquid beyond the flow point. Shear-thinning is beneficial for continuous extrusion during printing, as the decrease in viscosity with increasing shear rates facilitates flow through thin printing nozzles. The shear thinning behavior that arises from the introduction of solids, is due to the alignment of the anisotropic fillers and the break-up of particle agglomerates with increasing shear rate. At low stresses, the particle interactions prevent the paste from flowing until a stress beyond the material's flow point is applied.

hBN platelets alone, either S-BN or L-BN, create weak gels with relatively low flow points. S-BN/EP and L-BN/EP inks are particularly sensitive to the increase in frequency. It means they have low structural stability and are likely to exhibit phase separation or aggregation over time.[19] Even though the S-BN/EP and L-BN/EP inks have the same solid content and filler chemistry, their flow points and initial storage modulus were different. The higher storage modulus and flow points of the S-BN/EP paste could be related to the presence of S-BN particle agglomerates.
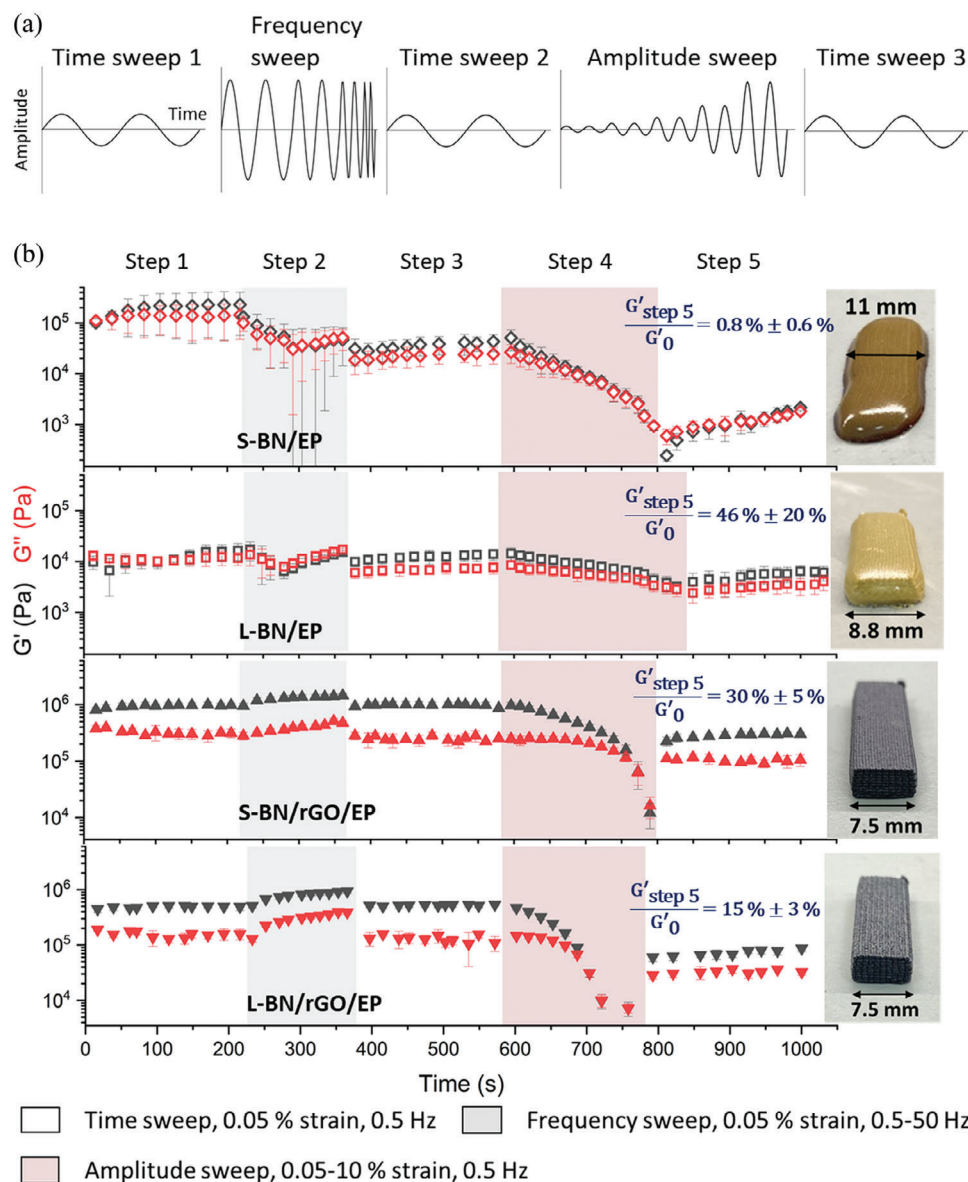
ADVANCED
SCIENCE NEWS

www.advancedsciencenews.com

ADVANCED
FUNCTIONAL
MATERIALS

www.afm-journal.de

Figure 2. a) Sinusoidal waves representing the oscillations applied to the pastes during the 5-step oscillatory sweeps. b) 5-step oscillatory sweep results for different hBN-containing EP pastes. Pictures of corresponding printed parts are inserted in each plot.

However, this interaction cannot be fully restored after they are broken under high shear strain as illustrated in the 5-step analysis in Figure 2, in which the viscous properties dominate at the beginning of step 5 and a 50–100 s period is required to recover a solid-like gel. The limited recovery could be attributed to the exfoliation and bending of hBN platelets under stress and challenges in re-forming the particle aggregates that contributed to establish the original structure.

A significant increase in the flow point was observed when rGO was incorporated into the ink due to the formation of a strong rGO network cooperating with hBN to support the structure. Inks with rGO exhibit higher viscosity at a given shear rate and stronger shear-thinning (lower n). This is caused by the formation of a physically entangled rGO network, which increases the viscosity of the paste but can be broken under high

shear rates. Graphene oxide (GO) works as a viscosifying agent in water-based DIW inks due to the strong chemical interaction (hydrogen bonding) between flakes triggering the formation a 3D liquid crystal structure in water.[18] However, the interaction between rGO flakes in the non-polar vitrimer is expected to be mainly through physical bonding.[21] The addition of rGO further increases the initial storage modulus and stress at the flow point and creates stronger gels. These gels are more difficult to break and retain their structures during the frequency sweep. The inks with rGO could not fully recover their storage modulus after disrupting their network due to potential irreversible changes, such as bending and breaking of hBN platelets and breaking of rGO flakes. However, the extent and speed of recovery were demonstrated to be sufficient for printing, according to the assessment of the shape retention capability of the printed structures.
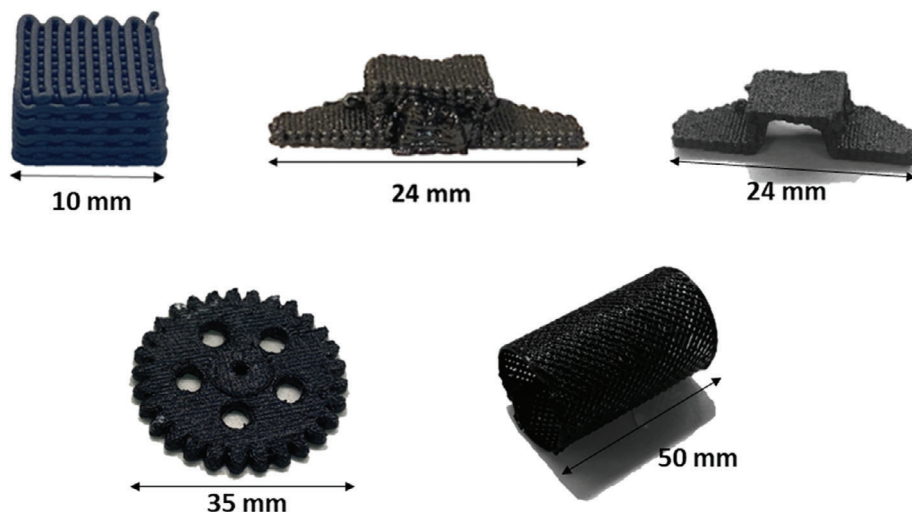
**ADVANCED
SCIENCE NEWS**

www.advancedsciencenews.com

**ADVANCED
FUNCTIONAL
MATERIALS**

www.afm-journal.de

Figure 3. Pictures of L-BN/rGO/EP parts produced via DIW: a) woodpile structure; b) as-printed "paper plane" with a support structure; c) cured "paper plane" where the support has been removed; d) dense gear with high shape fidelity and all the details retained after curing; e) tube made up by scrolling up a printed grid before curing.

Several printability criteria have been proposed for DIW inks. For example, Rocha et al.[15] demonstrated that a flow point higher than 500 Pa but lower than 2500 Pa is desired to ensure that the ink is self-supportive to maintain high shape fidelity while remaining extrudable without clogging the nozzle. Chan et al.[17] proposed another standard, where G' should recover to a value >10 000 Pa within 15 s after extrusion. According to both standards, inks containing rGO exhibit the properties required for good printability without slumping, which agrees with our observations during DIW. Rectangular bars printed with inks containing rGO exhibited excellent shape retention after printing and curing, while those printed using hBN/EP inks, regardless of the size of the hBN platelets, slumped after deposition.

Taking into account all the factors mentioned above, inks containing rGO were chosen to print EP-based hBN composites. Both S-BN/rGO/EP and L-BN/rGO/EP inks could be extruded stably and smoothly at a force of ≈75 N when using the 3 mL syringe and the 0.41 mm conical nozzle (Figure S6, Supporting Information). DIW of thermoset polymers to build grids or dense structures has been previously reported.[12,18] However, the printing of tall dense parts consisting of more than a few layers (printing height >2 mm) without the assistance of pre-curing, remains challenging, due to the need for high shape retention.[22] Our ink formulations not only enable the room temperature printing of hollow structures like the tube in **Figure 3e**, but also of tall 3D dense parts (printing height >3 mm), such as the gear in Figure 3d and the rectangular bars in the insets of Figure 2b. A woodpile structure can be readily printed (Figure 3), which is a demanding task using conventional resin casting methods. Typically, in the absence of appropriate support material, it is nearly impossible to build overhanging features using a basic DIW setup without combining printing with in situ UV or thermal-assisted curing.[23] Nonetheless, our system, with multiple printing nozzles, enables the printing of support structures using inks without hardener (4-AFD), which can be easily removed during post-processing, following an approach first suggested by Guo et al.[24] By employing multimaterial DIW, we were able to suc-cessfully print a "paper plane" with an overhang supported by a structure printed using the ink without hardener that remained soft after thermal curing and was removed with the aid of a spat-ula to extract the final component (Figure 3b,c).

2.2. Microstructure

In order to fabricate dense hBN/EP composites, the printing pattern has been adjusted to minimize the porosity by offsetting the extruded lines in adjacent layers. The densities of printed S-BN/rGO/EP and L-BN/rGO/EP composite parts are 1.47 ± 0.01 g cm^{-3} and 1.48 ± 0.01 g cm^{-3} respectively. Comparing them to their theoretical densities, the porosity has been estimated to be ≈2% for both materials.

The microstructure of single extruded filaments has been investigated using X-ray computed tomography (XCT) to visualize the orientation of hBN platelets. The XCT reconstructions in **Figure 4** showed that most L-BN platelets were longitudinally oriented, with few transversely oriented platelets. In contrast, the smaller hBN platelets show less pronounced alignment, although the resolution of the XCT was not sufficient to fully resolve neighboring particles in the 3D rendering. In addition, the distribution of both types of hBN fillers in the filament was inhomogeneous, the presence of hBN-free regions was observed in slices perpendicular and parallel to the extrusion direction (**Figure 5**).

The degree of orientation has been quantified using X-ray diffraction (XRD) of printed bars on planes parallel and perpendicular to the printing orientation, as illustrated in Figure 5, using:[25]

$$\delta = \frac{I_{(100)}}{I_{(100)} + I_{(002)}} \times 100\% \tag{2}$$

where δ represents the ratio of platelets that are vertically aligned to the face analyzed, $I_{(100)}$ is the intensity of the (100) peak and $I_{(002)}$ is the intensity of the (002) peak. The geometry of hBN
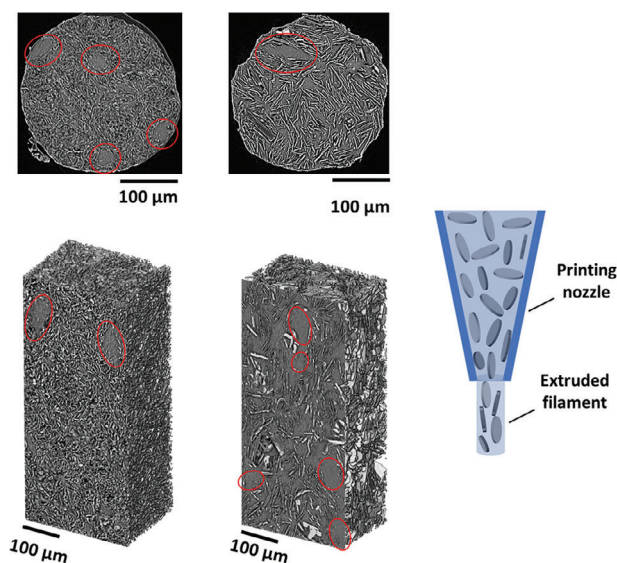
Figure 4. Reconstruction of a printed filament via XCT: a,b) slices perpendicular to the axial direction of L-BN/rGO/EP and S-BN/rGO/EP filaments respectively and c,d) 3D rendering of hBN platelets in S-BN/rGO/EP and L-BN/rGO/EP filaments with a slice parallel to the axial direction shown in the front. hBN-free regions on the slices were marked with red circles (the arrow indicates the extrusion direction). e) Illustration of the alignment of anisotropic platelets during extrusion through a thin nozzle.

platelets and corresponding crystal planes is illustrated in the inset of Figure 5. The (002) plane tends to orient parallel to the extrusion direction and the (100) plane tends to orient perpendicular to it, as evidenced by the values of δ obtained from XRD (Figure 5). Additionally, the composite containing larger hBN platelets exhibited a higher δ (43.0%) than the composite containing smaller platelets (34.2%) in agreement with the tomography observations.

The preferential alignment of hBN platelets was induced by the shear force exerted on them when extruding through the narrow DIW nozzle. The resulting torque rotates the platelets and aligns them in the direction of flow (Figure 4e). As the lateral size of fillers increases, the torque also increases. Therefore, under the same printing conditions, hBN platelets with larger basal faces are more likely to rotate and re-orient during extrusion, which results in a higher degree of orientation.[26]

2.3. Thermal Conductivities

hBN platelets have a high thermal conductivity ($\approx$200 W m^{-1} K^{-1}) in its planar direction across the (002) plane, but only $\approx$2 W m^{-1} K^{-1} in the thickness direction across the (100) plane.[27] The thermal conductivities of the composites built by DIW have been measured parallel (in-plane) and perpendicular (out-of-plane) to the printing direction (**Figure 6**b). The thermal conductivities of the composites in either direction were one order of magnitude higher than that of the neat EP (0.37 $\pm$ 0.03 W m^{-1} K^{-1}). Furthermore, their in-plane thermal conductivities were about twice the value of their out-plane ones. The in plane thermal conductivity of L-BN/rGO/EP (2.65 $\pm$ 0.16 W m^{-1} K^{-1}) is slightly lower than for S-BN/rGO/EP (3.09 $\pm$ 0.28 W m^{-1} K^{-1}) although the dif-

ferences are within the experimental error. These materials are electrical insulators. The resistance of the EP and its composites was beyond the multimeter's measurement limit (100 MΩ). The resistivities of the printed S-BN/rGO/EP and L-BN/rGO/EP composites were estimated to be >3.3 MΩ·m. The improvement in thermal transport has been visualized using an infrared camera. Bar surfaces perpendicular to the printing direction were heated together with a mold-casted EP sample. After heating for $\approx$30 s, the temperature distributions in the composite samples were more homogenous than that in the EP (Figure 6a).

The directional thermal transport can be explained by the preferential orientation of the hBN platelets in the printed parts. The theoretical thermal conductivities of a mixture with all the fillers connected and perfectly aligned, along (K_α) and perpendicular (K_β) to the alignment direction were estimated using the rule of mixtures, in which voids were not considered. Assuming that the effect of the rGO flakes was negligible because of their small content, for an EP composite with 22 vol.% of hBN, $K_\alpha \approx$44 W m^{-1} K^{-1} and $K_\beta \approx$0.37 W m^{-1} K^{-1}. Any hBN/EP composites with partially or randomly oriented hBN platelets should have thermal conductivities within this range. This simple model explains the difference in the thermal conductivities in the in-plane and out-of-plane directions of the printed composites. The percolation threshold of randomly oriented S-BN and L-BN were estimated to be 60 and 85 vol.%,[28] respectively. When the (002) plane normal of S-BN or L-BN platelets is aligned perpendicular to the extrusion direction, the value is reduced to roughly 3 vol.%. Our system lies between these two situations. Based on the degree of orientation calculated from the XRD spectra, an assumption was made that 40% of hBN platelets were perfectly aligned, which is $\approx$9 vol.% in the printed composites. This value is above the percolation threshold. However, the experimental values of the in-plane thermal conductivities were an order of magnitude below that of the predicted maximum. The contact between the platelets may not be good enough for efficient heat transfer due to factors such as the good wetting by the EP on hBN (Figure S14, Supporting Information). The difference in in-plane thermal conductivities between the hBN/EP composites with larger and smaller platelets are almost negligible considering experimental errors which is consistent with the small difference in the degree of orientation ($\approx$8.8%) and the variability in the intrinsic properties of the platelets. Our printed composites show superior in-plane thermal conductivities comparing to composite materials with similar hBN content (Figure 6c) produced by 3D-printing[29] or mold casting[30] reported in published works, but lower thermal conductivity than a hot-pressed hBN/epoxy material.[31] Hot-pressing might be more effective in inducing hBN alignment, which results in higher degree of filler orientation and a better conducting path.

There are two main approaches to obtain higher thermal conductivities in the printed hBN composites: 1) increasing the hBN content in the ink; 2) enhancing the hBN alignment to facilitate the in-plane thermal transport. The printability of the ink constrains the maximum hBN concentration and therefore enhancing alignment can be a more effective strategy. According to a previously published work by Feilden et al., the length of a cylindrical printing nozzle affects platelet alignment in the extruded filament.[32] This suggests the possibility of increasing the degree of hBN orientation in our composites by modifying the nozzle
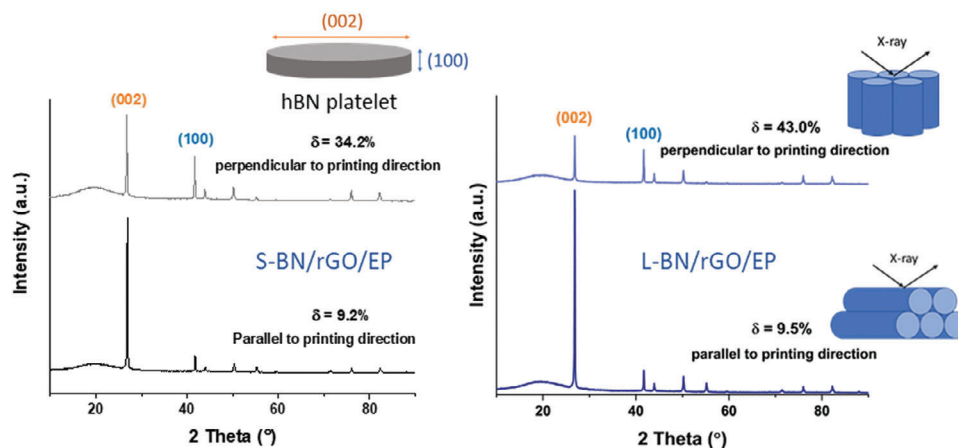
**ADVANCED
SCIENCE NEWS**

www.advancedsciencenews.com

**ADVANCED
FUNCTIONAL
MATERIALS**

www.afm-journal.de

Figure 5. XRD patterns of a) S-BN/rGO/EP and b) L-BN/rGO/EP printed bars on planes parallel or perpendicular to the printing direction. The inset on the left is an illustration of the geometry of a hBN platelet and corresponding crystal planes. The insets on the right are schematic representations of the of XRD analysis on the plane perpendicular (top) or parallel (bottom) to the printing orientation.

geometry. Adjustments to the ink rheology might be necessary to match the change in the nozzle. Our studies also show that alignment can be improved by increasing the platelet lateral size, but there is a practical limit in size given by the nozzle diameter. Other production methods, such as ice-templating or hot-pressing followed by epoxy resin infiltration, are more effective in achieving platelet alignment and can reach larger filler concentration but they require several processing steps and offer less design freedom.[31,33]

Taking advantage of the directional thermal transport in the composites, a heat concentrator ($20 \times 20 \times 3$ mm^3) was printed via DIW using the L-BN/rGO/EP ink.[34] The filaments were intentionally oriented toward the center, which created a cavity filled with neat EP after printing (**Figure 7**). When the concentrator was heated on a hot plate, an observable difference in temperature distribution was captured between the printed composite and the casted neat EP (Figure 7). The temperature at the center of the printed part was $\approx$10 °C higher than at the corners, indicating a localized heating effect. In contrast, the heat distribution in the casted EP part was more uniform, with a slightly cooler center. These results underline the potential of using the printed materials to direct heat flow and build thermal metamaterials for heat management.[34,35]

2.4. Mechanical Properties

After introducing hBN platelets into the EP matrix, the tensile and flexural modulus increased, while the strength decreased (**Table 1**). The inter-filament flexural strengths of printed materials were $\approx$60% of their trans-filament strengths. Moreover, the critical stress intensity factor (K_{IC}) and work of fracture calculated from single-edge notched bending (SENB) tests increased by adding hBN with the increase being higher for the composites with large platelets, L-BN/rGO/EP. For a brittle material with unstable fracture the work of fracture calculated from the area under the SENB force-displacement curves may contain some errors (**Figure 8**). Instead of that,

the facture energy of EP was calculated based on the following expression:[36]

$$G_{IC} = \frac{K_{IC}^2}{E} \tag{3}$$

The fracture surfaces have been examined under scanning electron microscope (SEM) (**Figure 9a–c**). The neat EP has a flat and smooth fracture surface without any visible pores, while those of hBN/EP composites are rather porous and rough. Furthermore, the composite containing larger hBN platelets was observed to have a rougher fracture surface.

The critical defect size, α, of the samples can be estimated using the Griffith/Irwin failure criterion:

$$K_{IC} = Y\sigma\sqrt{\pi\alpha} \tag{4}$$

where σ is the tensile strength and Y is a geometry factor, $\approx$1.[37] The critical defect size in EP was $\approx$10s of micrometers, while in the printed composites it was on the order of 10^2 μm.

To gain better understanding of mechanisms that generate fracture resistance in the materials we measured the dependence of the stress intensity factor, K_J, with crack length (**Figure 10**). While the EP is brittle, both composites exhibit a raising R-curve with toughness increasing with crack length until it reaches a plateau value for crack extensions of $\approx$0.5–1 mm.

As expected, the inclusion of hBN leads to an increase in the material stiffness due to the higher rigidity of the ceramic fillers when compared to the EP matrix and a decrease in the mechanical strength compared to the pure matrix because of the formation of defects, such as voids and weak hBN/EP interfaces. There was a large increment of one order of magnitude in the estimated critical defect size when comparing the neat EP to the printed composites. The presence of large defects, around hundreds of micrometers in size, in the printed composites was attributed to the big pores trapped between the printed lines. This led to an inter-filament strength lower than the trans-filament strength. Because of the high stiffness and shape retention of the pastes used for printing, the filaments could not slump and
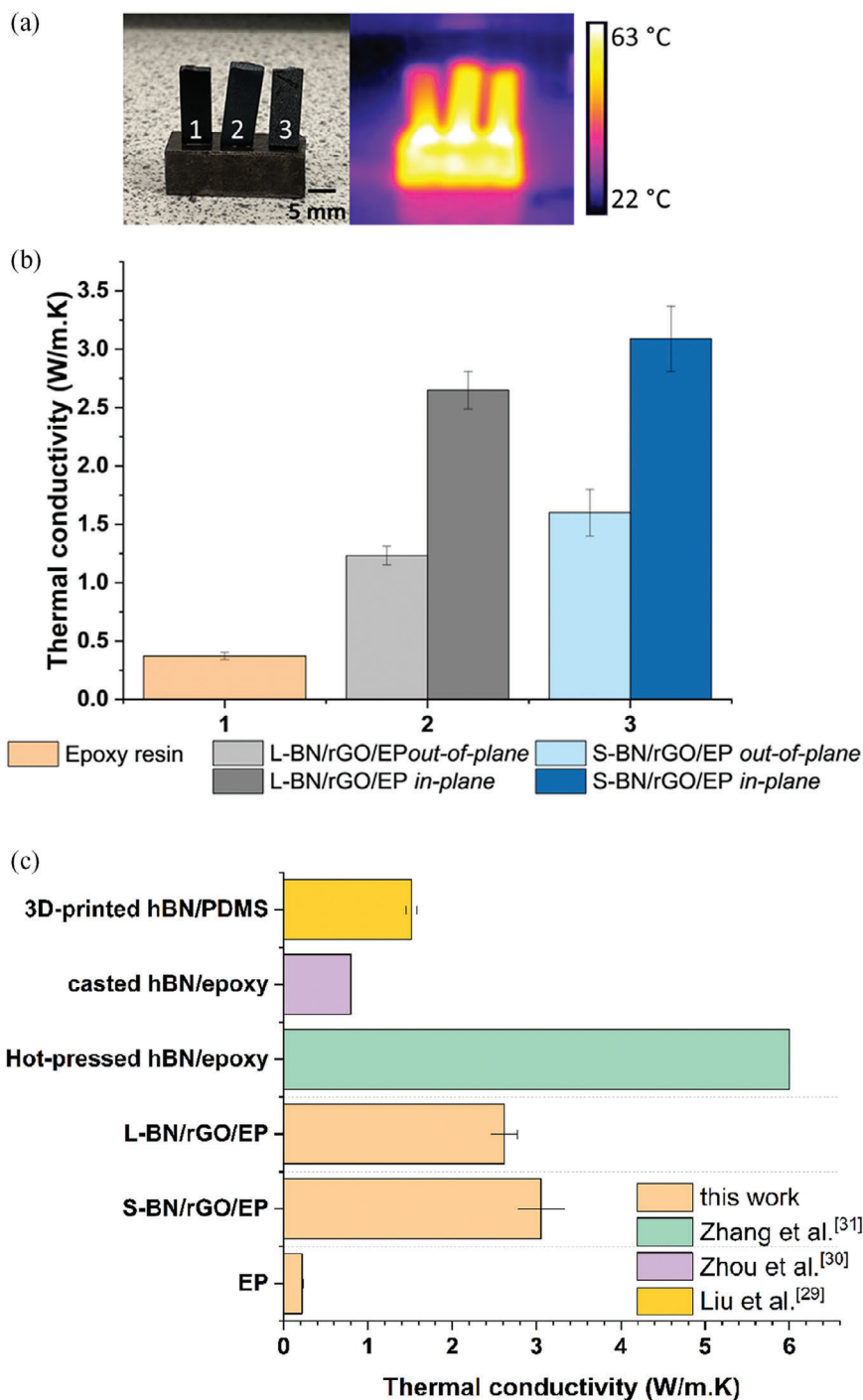
Figure 6. a) Infrared image taken on specimens (1: EP, 2: L-BN/rGO/EP, 3: S-BN/rGO/EP) fixed on a steel brick which has been heated on a hot-plate. b) Thermal conductivities of printed S-BN/rGO/EP and L-BN/rGO/EP in their in-plane and out-of-plane directions and of casted neat EP. c) Comparison of the thermal conductivities of rGO-modified EP-based hBN composites to similar materials reported in the literature. The hBN content in all these materials is ≈35 wt%.

fill completely the voids between them (Figure 9b,c). However, the resin is brittle, and the composites exhibit a more "graceful" failure with stable crack propagation, a gradual decrease of the stress strain curve and a raising R-curve behavior. The L-BN/rGO/EP composites exhibited the best crack resistance. They

have the highest K_{IC} and work of fracture and reached a K_J that is higher than the other two types of materials. This corresponds to an obviously rougher fracture surface when examined under SEM (Figure 9a–c). Mechanisms like crack deflection, bridging by the large platelets and platelet bending and exfoliation
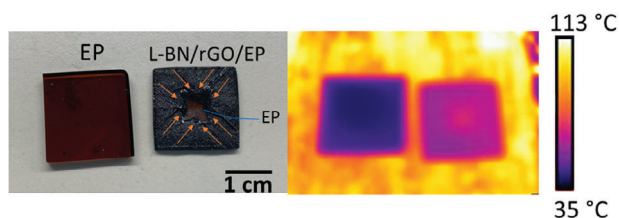
**ADVANCED
SCIENCE NEWS**

www.advancedsciencenews.com

**ADVANCED
FUNCTIONAL
MATERIALS**

www.afm-journal.de

Figure 7. Photograph of the casted EP and the printed L-BN/rGO/EP heat concentrator with its center cavity filled using neat EP after printing. The IR photograph on the left was taken after simultaneously heating the neat EP brick and the printed heat concentrator for 20 s on a hot plate (≈110 °C).

Table 1. Mechanical properties of mold-casted EP and printed hBN/rGO/EP composites.

Mechanical properties	EP	S-BN/rGO/EP	L-BN/rGO/EP
Tensile modulus/GPa	2.84 ± 0.35	4.55 ± 0.23	4.34 ± 0.39
Tensile strength-trans/MPa	53.4 ± 3.6	41.1 ± 4.5	32.3 ± 4.0
Tensile elongation at break/%	15.5 ± 2.6	1.4 ± 0.5	1.4 ± 0.2
Flexural modulus/GPa	2.22 ± 0.15	4.00 ± 0.32	4.21 ± 0.18
Flexural strength-trans/MPa	90.3 ± 7.5	68.8 ± 8.8	54.0 ± 3.1
Flexural strength-inter/MPa	–	43.9 ± 2.0	32.8 ± 4.7
Flexural strain at break/%	14.1 ± 2.4	2.3 ± 0.4	2.0 ± 0.4
K_{IC}/MPa·m$^{1/2}$	0.71 ± 0.07	1.19 ± 0.05	1.39 ± 0.01
Work of fracture/J m^{-2}	177.5 ± 39.3	124.3 ± 13.1	229.3 ± 54.2

contribute to the fracture energy and are more prevalent in materials with larger platelets (Figure 9d–f).

2.5. Reprocessability

The disulfide cross-linked EP utilized in this study is known for its recyclability and reprocessability. The 3D-printing of recyclable, nanoclay (≈10 vol.%) reinforced epoxy vitrimers has been reported before.[22b] However, the reprocessing of 3D-printed vitrimer-based composites with high filler content (>20 vol.%) remains largely unexplored. In order to assess the reprocessability
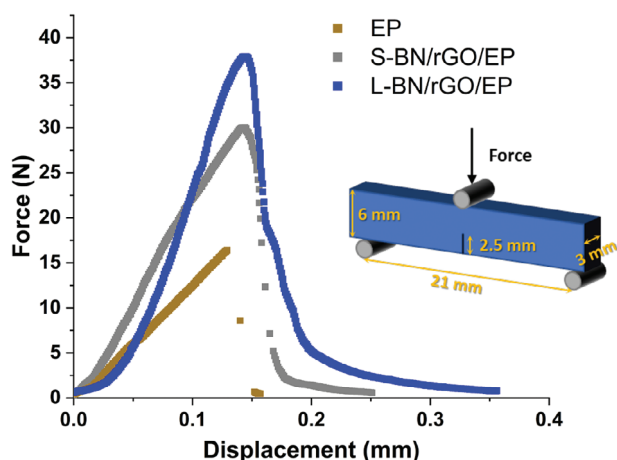

Figure 8. Force versus displacement graph from SENB tests. The inset is an illustration of the test setup and sample dimensions.

of printed and cured hBN/rGO/EP composites, fractured pieces were hot pressed into a plate, which was then cut and tested in 3-point bending to estimate the percentage of recovery in flexural modulus, flexural strength and strain at break. Results were compared to the neat EP. As shown in **Figure 11b**, the reprocessed EP and EP-based hBN composites have achieved full modulus recovery, and the recovery ratio in flexural strength was ≈80% for the neat EP and over 60% for both types of hBN/rGO/EP composites. The reprocessed EP exhibits a K_{IC} equivalent to the original material, while both types of composites showed K_{IC} values ≈80% of the as-printed ones. The recovery ratio in breaking strain for each material was comparable. It falls between 20% to 70%, considering the large error bars.

It is difficult to reach full recovery in strength and breaking strain after reprocessing even for the neat EP, given the possibility of trapping pores at the healed interfaces between fragments. Though the hot-pressing process minimize the voids between extruded filaments of printed composites as shown in the SEM images of fracture surfaces (Figure 11d,e), the new defects formed at partially healed interfaces resulted in a nearly double critical defect size than the original materials. The introduction of hBN further decreased healing due to the increase in viscosity, which hindered molecular movement and bond reformation. Moreover, hBN platelets broken during initial fracture could not be healed by hot pressing. This contributed to a reduction in fracture resistance and strength.

2.6. Shape Memory

The epoxy resin used in this work exhibits a thermally induced shape-memory effect which can be triggered by heating up beyond the glass transition temperature, T_g. The transition temperature, determined with differential scanning calorimetry (DSC), was ≈52 °C for all materials tested suggesting that the introduction of hBN and rGO did not affect the polymer structure (Figure S12, Supporting Information). To roughly evaluate the effect of hBN platelets on the shape recovery speed, a visual shape memory recovery assessment has been carried by heating each temporarily fixed specimen in a 60 °C water bath (Figure S13, Supporting Information). The recovery time for the printed S-BN/rGO/EP and L-BN/rGO/EP composite bars is roughly the same, they could recover from the bended "L" shape (≈90°) to a relatively straight shape (≈10°) in 6 s, while the pristine EP bar needed 9 s. At the very beginning of the heating process, the shape of the neat EP remained unchanged for ≈3 s. After 3 s, the shape recovery was activated and finished in 6 s. For the printed composite bars, recovery started in <1 s after immersing into the water bath.

Cyclic thermomechanical tests were used to assess the shape memory properties of printed composites. After the first cycle the strain response of the composites to the applied cyclic force and temperature became highly repeatable (**Figure 12b**). In Figure 12c,d, the percentage of shape fixity and recovery were calculated for each cycle and compared to those of the neat EP reported by Azcune et al.[38] The recovery of the EP in the first cycle is higher than that in the published work[38] due to the method used in the calculation, but consistent in the following cycles. The composites possess excellent fixity up to ≈85%. The

ADVANCED
SCIENCE NEWS
www.advancedsciencenews.com

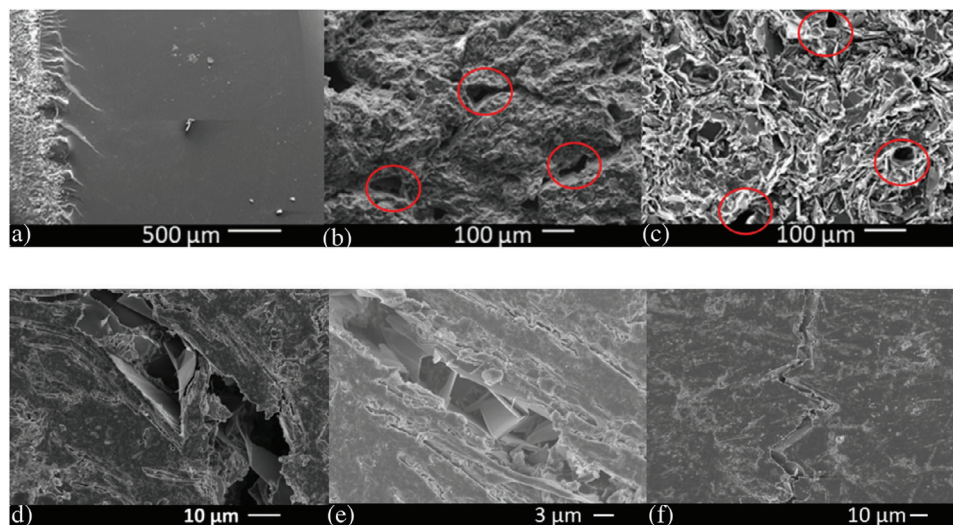**ADVANCED**
FUNCTIONAL
MATERIALS
www.afm-journal.de

Figure 9. a–c) SEM images of the fracture surfaces of a) neat EP, b) S-BN/rGO/EP, and c) L-BN/rGO/EP after SENB. Voids trapped between extruded lines are marked with red circles. d–f) SEM images of a crack that propagated through the L-BN/rGO/EP composites during SENB. The exfoliation and bending of L-BN platelets are clearly visible in (d) and (e). This kind of toughening mechanism has not been observed in S-BN/rGO/EP specimens. Crack deflection is shown in (f).

incorporation of hBN platelets promotes shape fixity in all the testing cycles by more than 30% (Figure 12c). When looking at the shape recovery ratio, the pure EP and composites showed similar performance. In cycle 1, each material exhibits a recovery ratio lower than the following cycles with large error bars. In cycle 2 and 3, the recovery ratio of the three materials remained constant between 90% and 100%. A further fourth cycle has been done with the composites with no obvious decline in the recovery. The shape memory effect can be combined with the DIW design to develop different configurations. For example, in Figure 12a the wing position of the "paper plane" printed via multimaterial DIW was altered based on the shape programming and recovery process. In addition, a printed tube, which was squeezed into an elliptical tube at $T > T_g$, could recover to its original cylindrical shape upon reheating (Figure 12b).

The time taken for the thermal-activated shape recovery in a polymer depends on two main factors: the speed of heat trans-fer in the material and the type of switching mechanism – glass transition or melting. In our case, all the materials undergo their glass transition within the same temperature range (Figure S11, Supporting Information). Therefore, the thermal conductivity is the main rate-controlling factor. The difference between the shape transformation is due to the time taken for the heat to transport throughout the bar to reach the aimed T_g. The delay in the shape memory response is a common problem for SMPs, because of their poor thermal conductivities. This can be more obvious in larger parts, which require longer time to reach the switching temperature. For applications demanding rapid shape change response, this delay is fatal. Thanks to the enhanced rate of thermal transfer led by introducing hBN fillers, the time taken to initiate the shape transformation in the composites has been shortened to less than a third of that of the original EP.

High shape fixity and recovery ratio are desired for shape memory materials. The higher fixity ratio in hBN/EP composites that in pure EP can be explained by the increase in the stiffness from the rigid hBN platelets which hinder the movement and rearrangement of polymer chains after deforming and fixing at temporary shapes. For all materials, the recovery ratio in the first cycle is lower than the following cycles, because it involves unrecoverable plastic deformation and formation of defects under stress. This also leads to a large error bar in the calculated value of the cycle 1 recovery ratio. In the following cycles, the consistent shape recovery ratio of the composites compared to the pure EP demonstrates that the introduction of hBN and rGO fillers did not compromise the shape memory ability of the matrix material.

3. Conclusion

In this work we demonstrate the room temperature 3D printing of shape memory epoxy vitrimer-based hBN composites
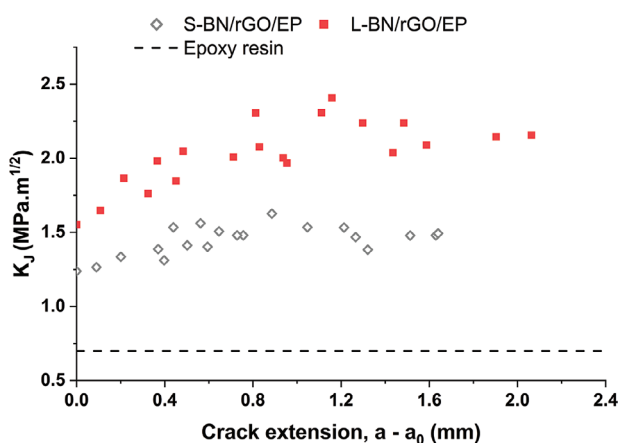

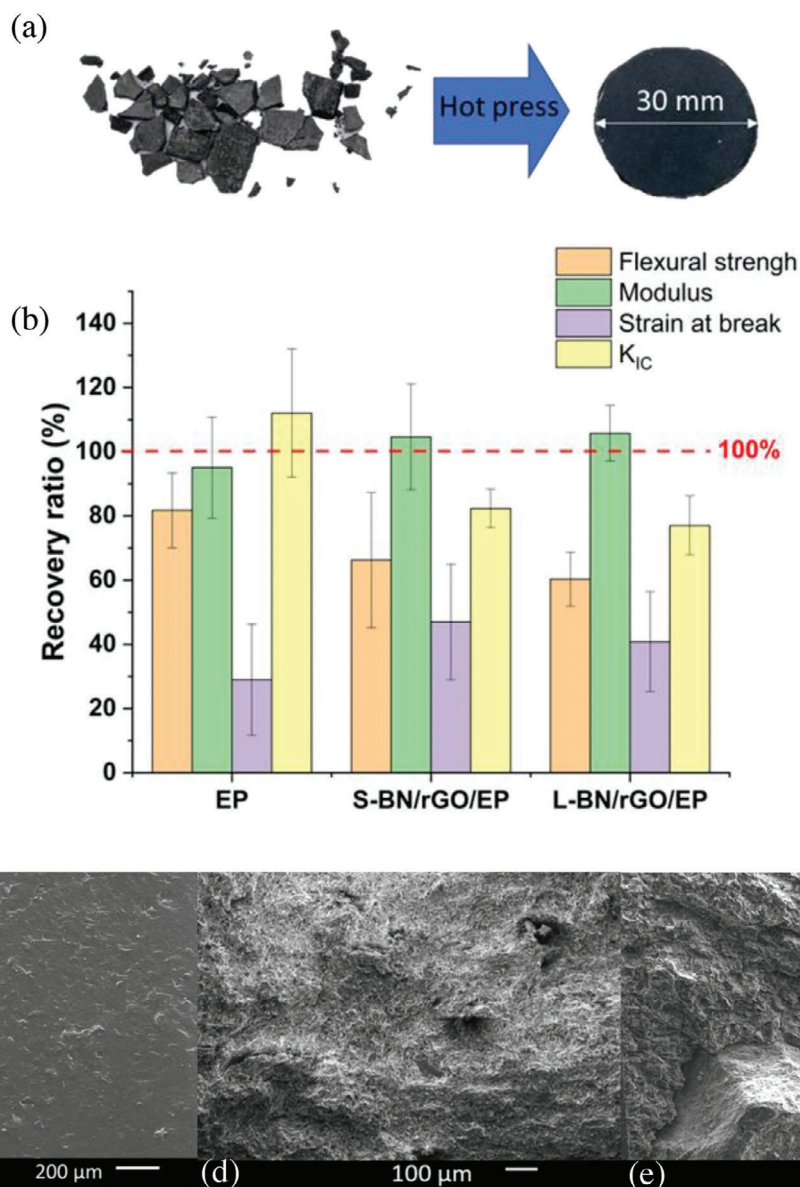**Figure 10.** R-curves of neat EP, S-BN/rGO/EP and L-BN/rGO/EP.

Figure 11. Reprocessing of the pure EP and EP-based printed composites: a) Images illustrating the reprocessing via hot pressing of L-BN/rGO/EP composites. The specimens were broken into small pieces which were pressed at 190 °C and 20 MPa for 40 min into a 30 mm diameter plate. b) Recovery ratio in flexural modulus, flexural strength, strain at break and K_{IC} after reprocessing. SEM images c–e) of the fracture surface of reprocessed materials: c) EP, d) S-BN/rGO/EP, and e) L-BN/rGO/EP after SENB. A defect formed at partially healed interface is marked with a red circle.

usingDIW. By incorporating rGO and hBN fillers, printing inks with high shape retention capability were formulated. The alignment of hBN platelets during printing led to directional thermal transport, with in-plane conductivities reaching ≈3 W m⁻¹ K⁻¹. This value was approximately one order of magnitude higher than the neat EP. The enhancement in thermal conductivities speeds the thermally activated shape memory process and the combination of additive manufacturing with directional conductivity enables the design of thermal metamaterial structures. Furthermore, the addition of hBN results in the development of toughening mechanisms that increase the fracture resistance of the material while retaining the shape memory capabilities of the EP matrix and similar strengths. The nature of the atomic bond-

ing in the vitrimer matrix enables the reprocessing and reuse of printed structures to fabricate new parts that retain a significant amount of strength (over 60%).

4. Experimental Section

Materials: The EP was prepared using DGEBA-based epoxy resin (ARALDITE LY1564) purchased from Huntsman Advanced Materials, DGEPPG (M_n = 380; epoxy equivalent weight of 190 g eq⁻¹) purchased from Sigma Aldrich, and 4-AFD (≥98.0%) (Figure S1, Supporting Information). GO was prepared using graphite flakes (SKU332461, 150–500 μm sieved, Sigma Aldrich). hBN platelets in two different particle sizes, d(50) = 6 μm (AB134567, abcr, density = 2.37 g cm⁻³) marked as S-BN in this
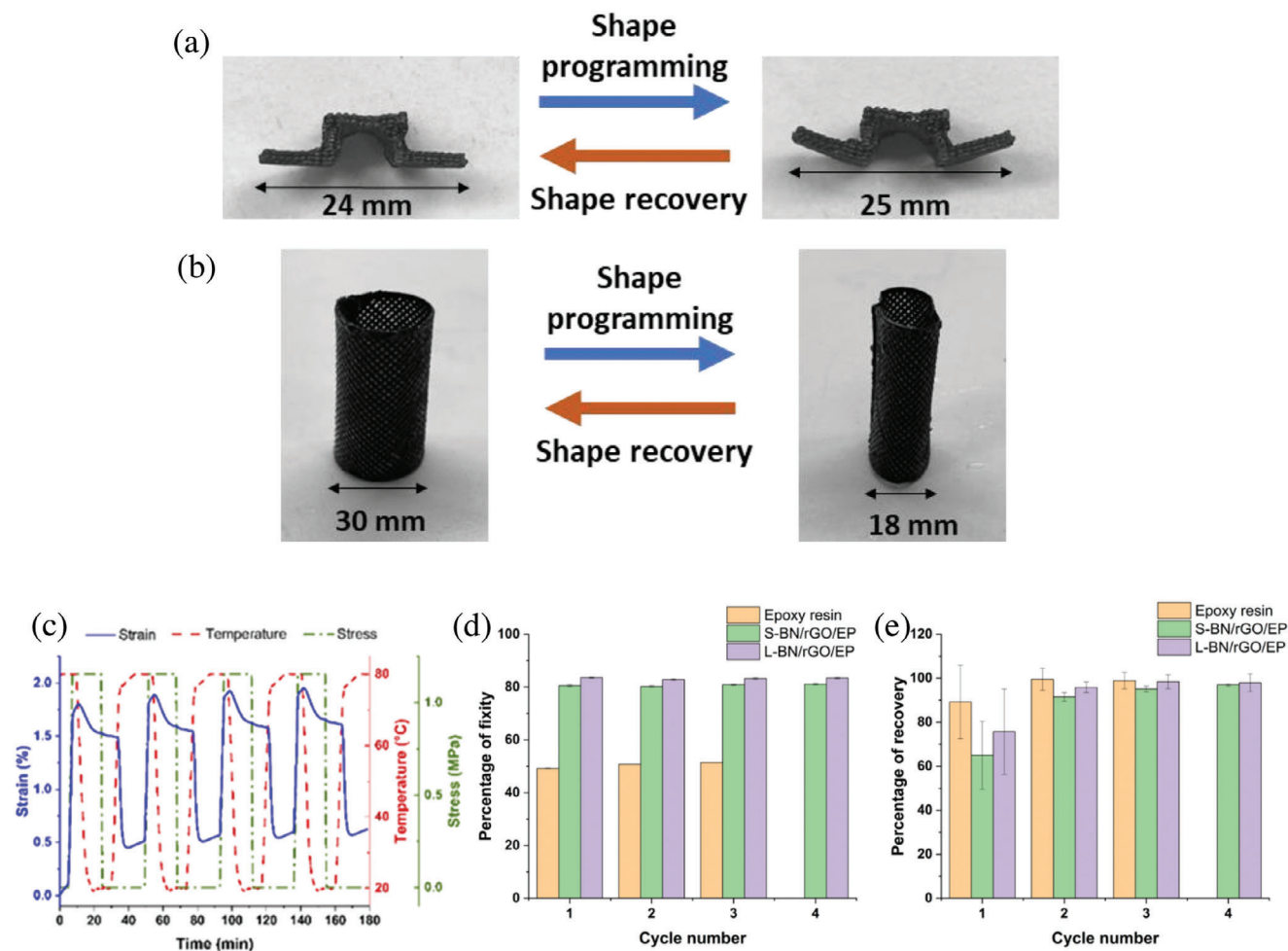
Figure 12. Shape memory behavior of the EP and EP-based printed composites: Transformation of a) wing configurations in a printed sample (see Figure 3) and b) expansion of a printed tube (see Figure 3) based on the shape memory effect. c) Quantitative analysis of shape memory performance for L-BN/rGO/EP. Comparison of calculated d) fixities and e) recoveries of hBN composites and the neat EP.

work and d(50) = 25 µm (SP30, Saint Gobain, density = 2.2 g cm^{-3}) denoted as L-BN have been used (Figure S2, Supporting Information).

rGO Synthesis: GO water suspensions were synthesized using the Modified Hummers' method[39] to chemically exfoliate graphite in a 5L reactor. The suspensions were centrifuged at 8000 rpm for 30 min while being rinsed with deionized water to eliminate any unreacted chemicals. GO suspensions with a pH ≈6 were obtained after more than 15 cycles of centrifugation. The GO water suspension was dried in a convection oven for 48 hours at 37 °C. After drying, the graphene oxide was reduced by microwave irradiation in air for two minutes in a microwave oven (1000 W, Daewoo electronics) to produce rGO. Raman spectra of the GO and rGO provided in Figure S3 (Supporting Information).

EP Preparation: DGEPPG and DGEBA were mixed by centrifugal mixing (ARE-250, Thinky, USA) at 2000 rpm at a weight ratio of 23:77. The hardener 4-AFD was added to the mixture after it had been thoroughly mixed, and it was dissolved at 80 °C. The mixture and hardener were weighted at 100:37. The homogeneous mixture was defoamed for 10 min at 2200 rpm in a Thinky Mixer, and then it was further degassed in a vacuum desiccator until no discernible air bubbles remained. Pristine epoxy components were casted in silicone moulds, cured at 120 °C for 2.5 h, and then post-cured at 150 °C for 2 h.

Paste Preparation: Feed-stock pastes were prepared by dispersing the hBN platelets and rGO in the pre-mixed EP through a series of 2-minute mixing cycles with the Thinky Mixer at 2000 rpm until the flakes were fully incorporated. Degassing took place at 2200 rpm for 20 min. The EP slurries containing 27 vol.% of smaller (6 µm) or larger (25 µm) hBN are named S-BN/EP and L-BN/EP respectively, while the one containing hBN (6 µm) and rGO is denoted as S-BN/rGO/EP. Similarly, the paste composed of hBN (25 µm) and rGO was named L-BN/rGO/EP.

DIW of Composites: A 3 ml syringe barrel, equipped with a 410 µm diameter printing nozzle, was filled with the slurry. The direct ink writing process was conducted at room temperature using a Robocaster system (3dInks, USA). The ink was deposited layer by layer onto a PTFE substrate, while continuously extruding from the nozzle at a speed of 6 mm s^{-1}. The z-axis spacing was set to 340 µm and an x-axis offset of half the extruded filament diameter (205 µm) to reduce the pores trapped between filaments and increase the density of printed parts. The printing designs are presented in supporting information (Figure S5, Supporting Information). A hollow tube structure was built by printing a double layer grid onto a piece of paper which was then scrolled up into a tube. The paper was removed after curing. The printed parts underwent a thermal curing at 120 °C for 2.5 h and a post-curing at 150 °C for 2 h.

Rheology of Pastes: The rheological behavior of the pastes was investigated in a TA HR1 rheometer using a plate geometry (Ø = 40 mm) with a 1500 µm gap at a temperature of 25 °C. Flow ramp and oscillatory amplitude sweep tests were carried on at a frequency of 0.5 Hz. For flow ramps, the shear rates were ranging from 0.1 to 30 s^{-1}. To further evaluate the

**ADVANCED
SCIENCE NEWS**

www.advancedsciencenews.com

**ADVANCED
FUNCTIONAL
MATERIALS**

www.afm-journal.de

structural evolution under different rheological stimuli, 5-step oscillatory sweeps have been used. They consist of a time sweep with a low fixed oscillation strain (0.05% strain) at the beginning of the test to estimate the original properties of the paste at a relatively stationary state, a frequency sweep to determine the stability of the sample under an increasing oscillation frequency, a second time sweep to assess the reconstruction of network after step 2, an amplitude sweep to simulate the yielding or breaking of the ink structure when printing, and a final time sweep at 0.05% strain to compare with the initial step and quantify structural recovery in the paste.

Reprocessing: In order to evaluate the reprocessing capabilities of the materials, fractured pieces of printed and fully cured specimens were pressed under 20 MPa pressure in a graphite die and heated at 190 °C for 40 min to reform into a 30 mm diameter, ≈2.5 mm thick plate using a uniaxial hot press.

Mechanical Properties: Tensile, 3-point bending and SENB tests have been done to compare the mechanical performance of the printed hBN/EP composites to the casted neat EP. Mechanical tests were carried using a microtest stage (MT300 Tensile Tester, DEBEN, UK). In all the mechanical tests, neat epoxy resin specimens were prepared through mold-casting, while hBN composites were fabricated using direct ink writing. For tensile tests, dog-bone (gauge length = 6 mm) specimens were used. The tension was applied in a direction parallel to the extruded lines (trans-filament fracture). For 3-point bending tests, all the as-casted and as-printed specimens were made into rectangular bars with dimensions of $4 \times 4 \times 32$ mm^3 and tested with a support span of 21 mm. All specimens were ground and polished to remove large surface defects. The flexural strengths of the printed composites were tested in trans-filament and inter-filament (tension applied perpendicular to the extruded lines) configurations. Reprocessed neat EP and composite plates were cut into rectangular bars with dimensions of $2.5 \times 3 \times 25$ mm^3 and tested in bending with a support span of 16.5 mm. For SENB tests, rectangular bars with dimensions of $3 \times 6 \times 32$ mm^3 were prepared, which were then notched by cutting with a SiC wafer blade in the direction perpendicular to the filament orientations to induce trans-filament fracture, which was followed by notch sharpening with a razor blade. The depth of the notch was between 2 and 3 mm and the span was 21 mm. An optical camera was used to record the crack propagation and to plot the R-curve following the ASTM E1830 standard (see Supporting Information). The machine crosshead moving speed was 0.1 mm min^{-1} for all mechanical measurements.

Thermal Conductivity Measurements: The thermal conductivities were calculated using the following equation:

$$K = D\rho C_p \tag{5}$$

where K is the thermal conductivity, D is the thermal diffusivity, ρ is the density of the specimen and C_p is the specific heat capacity. D was measured at room temperature (≈22 °C) using the laser flash technique (LFA 427, NETZSCH, GE), and C_p was determined using the method described in the ASTM E1269−11 standard with a Mettler Toledo 3 Star DSC.

For each material the difference in thermal conductivities was visualized by recording the thermal images of a rectangular bar ($6 \times 3 \times 15$ mm^3) heated from the bottom end for 30s on a hot plate with FLIR E52 infrared camera.

Thermomechanical Analysis: The shape memory properties of printed hBN/rGO/EP composites were tested using a TA Instruments DMA Q800 system under controlled force mode with a tensile film fixture. The specimens were printed into $12 \times 1.5 \times 17.5$ mm^3 plates. The samples were heated from room temperature to 80 °C at 10 °C min^{-1}, then uniaxial tensile loading was applied at 5 N/min until reaching 12 N. The force was held for 5 min. After that, the sample was released at a rate of 5 N min^{-1} until it was stress free. This process was repeated three times and the strain was recorded.

From the thermomechanical cycles, fixity, R_f, and recovery ratio, R_r, in each cycle can be calculated as:

$$R_f(N) = \frac{\varepsilon_u(N)}{\varepsilon_m(N)} \tag{6}$$

$$R_r(N) = \frac{\varepsilon_m(N) - \varepsilon_r(N)}{\varepsilon_m(N) - \varepsilon_r(N-1)} \tag{7}$$

where N is the cycle number, ε_m is the maximum strain reached in a certain cycle, ε_u is the strain of the temporary shape fixed at room temperature after unloading the sample and ε_r is the strain recorded at the stress-free state after recovering from its temporary shape. Indication of ε_m, ε_u and ε_r in cycle N of thermomechanical test curves is provided in Figure S10 (Supporting Information).

Electrical Resistivity Measurement: The electrical resistivity of printed parts (dimensions: $10 \times 10 \times 3$ mm^3) was measured using a Tektronix DMM4020 digital multimeter in two probe method.

Visual Shape Memory Test: Mold-casted pristine EP and printed hBN/EP composites were prepared in the form of rectangular bars with dimensions of $2 \times 6 \times 30$ mm. They were bent into an "L" shape upon heating in a water bath at 60 °C, followed by fixing their temporary shape by cooling them down to room temperature with running tap water. The shape recovery process of each specimen was triggered by immersing the bent bar in the 60 °C water bath again. The process was video recorded.

XRD: XRD patterns of printed BN composites were taken on a Bruker D2 PHASER diffractometer using Cu Kα radiation. The diffraction angle, 2θ, varied between 10° and 90°. Scan step size was 0.034° and the step time was set to 76.8 s.

XCT: Printed and cured single S-BN/rGO/EP and L-BN/rGO/EP filaments (≈0.4 mm in diameter) were cut to a length of 3 mm and mounted onto acrylic rods using superglue and analysed using x-ray tomography in a ZEISS Xradia Versa 620 x-ray microscope. The specimen was placed at 8 mm away from the detector and 8 mm away from the X-ray source. An optical magnification of ×20 was used for the experiment. The X-ray source was operating at 60 keV with a current of 108 µA. For the CT scan, the radiograph exposure time was 5 s, and 3200 projections were taken. This resulted in an effective pixel size of 0.338 µm.

SEM: The fracture surfaces of specimens after SENB tests were observed using a JEOL 6010 SEM with secondary electrons. A gold coating was applied to the surface before examining under SEM. The crack path in printed samples were checked using a Zeiss Auriga SEM. A chromium coating was applied to the sample surface.

Supporting Information

Supporting Information is available from the Wiley Online Library or from the author.

Acknowledgements

Conflict of Interest

The authors declare no conflict of interest.

Data Availability Statement

The data that support the findings of this study are available from the corresponding author upon reasonable request.

[1] a) W. J. Renton, *Int. J. Solids Struct.* **2001**, *38*, 3309; b) M. M. Williams Tiffany, S. Miller, S. Daniel, in *Society of Advanced Materials Processing and Engineering (SAMPE)*, Forth Worth, TX, USA, October **2011**.

[2] E. A. Ott (Ed.), *Shape Changing Airfoil*, No. NASA/CR-2005-213971, **2005**.

[3] H. Lu, K. Yu, Y. Liu, J. Leng, *Smart Mater. Struct.* **2010**, *19*, 065014.

[4] a) W. Small, P. R. Buckley, T. S. Wilson, W. J. Benett, J. Hartman, D. Saloner, D. J. Maitland, *IEEE Trans. Biomed. Eng.* **2007**, *54*, 1157; b) H. Wache, D. Tartakowska, A. Hentrich, M. Wagner, *J. Mater. Sci.: Mater. Med.* **2003**, *14*, 109.

[5] L. Santo, F. Quadrini, A. Accettura, W. Villadei, *Proc. Eng.* **2014**, *88*, 42.

[6] M. Irie, K. Otsuka, C. Wayman, *Shape Memory Materials*, Cambridge University Press, Cambridge, UK, **1998**, 203.

[7] Z. Wang, Z. Wu, L. Weng, S. Ge, D. Jiang, M. Huang, D. M. Mulvihill, Q. Chen, Z. Guo, A. Jazzar, X. He, X. Zhang, B. B. Xu, *Adv. Funct. Mater.* **2023**, *33*, 2301549.

[8] H. He, W. Peng, J. Liu, X. Y. Chan, S. Liu, L. Lu, H. Le Ferrand, *Adv. Mater.* **2022**, *34*, 2205120.

[9] H. Meng, G. Q. Li, *Polymer* **2013**, *54*, 2199.

[10] a) H. B. Lu, Y. J. Liu, J. H. Gou, J. S. Leng, S. Y. Du, *Smart Mater. Struct.* **2010**, *19*, 075021; b) H.-F. Lee, H. H. Yu, *Soft Matter* **2011**, *7*, 3801.

[11] H. Koerner, G. Price, N. A. Pearce, M. Alexander, R. A. Vaia, *Nat. Mater.* **2004**, *3*, 115.

[12] S. Chandrasekaran, E. B. Duoss, M. A. Worsley, J. P. Lewicki, *J. Mater. Chem. A* **2018**, *6*, 853.

[13] J. P. Lewicki, J. N. Rodriguez, C. Zhu, M. A. Worsley, A. S. Wu, Y. Kanarska, J. D. Horn, E. B. Duoss, J. M. Ortega, W. Elmer, R. Hensleigh, R. A. Fellini, M. J. King, *Sci. Rep.* **2017**, *7*, 43401.

[14] a) A. Corker, H. C.-H. Ng, R. J. Poole, E. García-Tuñón, *Soft Matter* **2019**, *15*, 1444; b) A. M'barki, L. Bocquet, A. Stevenson, *Sci. Rep.* **2017**, *7*, 6017.

[15] V. G. Rocha, E. Saiz, I. S. Tirichenko, E. García-Tuñón, *J. Mater. Chem. A* **2020**, *8*, 15646.

[16] N. S. Hmeidat, J. W. Kemp, B. G. Compton, *Compos. Sci. Technol.* **2018**, *160*, 9.

[17] S. S. L. Chan, M. L. Sesso, G. V. Franks, *J. Am. Ceram. Soc.* **2020**, *103*, 5554.

[18] J. N. Rodriguez, C. Zhu, E. B. Duoss, T. S. Wilson, C. M. Spadaccini, J. P. Lewicki, *Sci. Rep.* **2016**, *6*, 27933.

[19] E. Garcia-Tunon, E. Feilden, H. Zheng, E. D'Elia, A. Leong, E. Saiz, *ACS Appl. Mater. Interfaces* **2017**, *9*, 32977.

[20] J. A. Lewis, *J. Am. Ceram. Soc.* **2000**, *83*, 2341.

[21] a) J. R. Potts, D. R. Dreyer, C. W. Bielawski, R. S. Ruoff, *Polymer* **2011**, *52*, 5; b) L.-C. Tang, Y.-J. Wan, D. Yan, Y.-B. Pei, L. Zhao, Y.-B. Li, L.-B. Wu, J.-X. Jiang, G.-Q. Lai, *Carbon* **2013**, *60*, 16.

[22] a) M. Cheng, A. Ramasubramanian, M. G. Rasul, Y. Jiang, Y. Yuan, T. Foroozan, R. Deivanayagam, M. Tamadoni Saray, R. Rojaee, B. Song, V. R. Yurkiv, Y. Pan, F. Mashayek, R. Shahbazian-Yassar, *Adv. Funct. Mater.* **2021**, *31*, 2006683; b) Q. Shi, K. Yu, X. Kuang, X. Mu, C. K. Dunn, M. L. Dunn, T. Wang, H. Jerry Qi, *Mater. Horiz.* **2017**, *4*, 598.

[23] K. Chen, X. Kuang, V. Li, G. Kang, H. J. Qi, *Soft Matter* **2018**, *14*, 1879.

[24] Y. Guo, Y. Liu, J. Liu, J. Zhao, H. Zhang, Z. Zhang, *Composites, Part A* **2020**, *135*, 105903.

[25] T. Fujihara, H.-B. Cho, T. Nakayama, T. Suzuki, W. Jiang, H. Suematsu, H. D. Kim, K. Niihara, *J. Am. Ceram. Soc.* **2012**, *95*, 369.

[26] R. L. Walton, E. R. Kupp, G. L. Messing, *J. Mater. Res.* **2021**, *36*, 3591.

[27] M. Tanimoto, T. Yamagata, K. Miyata, S. Ando, *ACS Appl. Mater. Interfaces* **2013**, *5*, 4374.

[28] J. Li, J.-K. Kim, *Compos. Sci. Technol.* **2007**, *67*, 2114.

[29] M. Liu, S.-W. Chiang, X. Chu, J. Li, L. Gan, Y. He, B. Li, F. Kang, H. Du, *Ceram. Int.* **2020**, *46*, 20810.

[30] W. Zhou, J. Zuo, X. Zhang, A. Zhou, *J. Compos. Mater.* **2014**, *48*, 2517.

[31] T. Zhang, J. Sun, L. Ren, Y. Yao, M. Wang, X. Zeng, R. Sun, J.-B. Xu, C.-P. Wong, *Composites, Part A* **2019**, *121*, 92.

[32] E. Feilden, C. Ferraro, Q. Zhang, E. García-Tuñón, E. D'elia, F. Giuliani, L. Vandeperre, E. Saiz, *Sci. Rep.* **2017**, *7*, 13759.

[33] X. Zeng, Y. Yao, Z. Gong, F. Wang, R. Sun, J. Xu, C.-P. Wong, *Small* **2015**, *11*, 6205.

[34] K. P. Vemuri, F. Canbazoglu, P. R. Bandaru, *Appl. Phys. Lett.* **2014**, *105*, 193904.

[35] a) G. Dai, J. Huang, *J. Appl. Phys.* **2018**, *124*, 235103; b) J. Wang, G. Dai, J. Huang, *iScience* **2020**, *23*, 101637.

[36] W. J. Clegg, K. Kendall, N. M. Alford, T. W. Button, J. D. Birchall, *Nature* **1990**, *347*, 455.

[37] S. Strobl, P. Supancic, T. Lube, R. Danzer, *J. Eur. Ceram. Soc.* **2012**, *32*, 1491.

[38] I. Azcune, A. Huegun, A. R. de Luzuriaga, E. Saiz, A. Rekondo, *Eur. Polym. J.* **2021**, *148*, 110362.

[39] D. C. Marcano, D. V. Kosynkin, J. M. Berlin, A. Sinitskii, Z. Sun, A. Slesarev, L. B. Alemany, W. Lu, J. M. Tour, *ACS Nano* **2010**, *4*, 4806.